White Rose Research Online

eprints@whiterose.ac.uk
https://eprints.whiterose.ac.uk
Universities of Leeds, Sheffield and York

Deposited via The University of York.

White Rose Research Online URL for this paper:
https://eprints.whiterose.ac.uk/id/eprint/221490/

Version: Published Version

Article:
Jones, Harriet, Kumar, Ashish, O'Leary, Catherine et al. (2024) Experimental and Computational Investigation of the Emission and Dispersion of Fine Particulate Matter (PM2.5) During Domestic Cooking. Atmosphere. 1517. ISSN: 2073-4433

https://doi.org/10.3390/atmos15121517

Reuse
This article is distributed under the terms of the Creative Commons Attribution (CC BY) licence. This licence allows you to distribute, remix, tweak, and build upon the work, even commercially, as long as you credit the authors for the original work. More information and the full terms of the licence here: https://creativecommons.org/licenses/

Takedown
If you consider content in White Rose Research Online to be in breach of UK law, please notify us by emailing eprints@whiterose.ac.uk including the URL of the record and the reason for the withdrawal request.

UNIVERSITY OF LEEDS
University of Sheffield
UNIVERSITY of York

atmosphere

MDPI

Article

Experimental and Computational Investigation of the Emission and Dispersion of Fine Particulate Matter ($PM_{2.5}$) During Domestic Cooking

Harriet Jones [1,*], Ashish Kumar [2], Catherine O'Leary [2], Terry Dillon [2] and Stefano Rolfo [1]

[1] Scientific Computing, Daresbury Laboratory, Science and Technology Facilities Council, UKRI, Warrington WA4 4AD, UK; stefano.rolfo@stfc.ac.uk
[2] Wolfson Atmospheric Chemistry Laboratories, Department of Chemistry, University of York, York YO10 5DQ, UK; ashish.kumar@york.ac.uk (A.K.); catherine.oleary@york.ac.uk (C.O.); terry.dillon@york.ac.uk (T.D.)
* Correspondence: harriet.jones@stfc.ac.uk

Abstract: As the wealth of evidence grows as to the negative impact of indoor air quality on human health, it has become increasingly urgent to investigate and characterise sources of air pollution within the home. Fine particulate matter with a diameter of 2.5 µm or less ($PM_{2.5}$) is a key cause for concern, and cooking is known to be one of the most significant sources of domestic $PM_{2.5}$. In this study, the aim was to demonstrate the efficacy of combining experimental techniques and cutting-edge High-Performance Computing (HPC) to characterise the dispersion of $PM_{2.5}$ during stir-frying within a kitchen laboratory. This was carried out using both experimental measurement with low-cost sensors and high-fidelity Computational Fluid Dynamics (CFD) modelling, in which Lagrangian Stochastic Methods were used to model particle dispersion. Experimental results showed considerable spatio-temporal variation across the kitchen, with $PM_{2.5}$ mass concentrations in some regions elevated over 1000 µg m^{-3} above the baseline. This demonstrated both the impact that even a short-term cooking event can have on indoor air quality and the need to factor in such strong spatio-temporal variations when assessing exposure risk in such settings. The computational results were promising, with a reasonable approximation of the experimental data shown at the majority of monitoring points, and future improvements to and applications of the model are suggested.

Keywords: particulate matter; sensors; mass concentration; computational fluid dynamics

check for updates

Citation: Jones, H.; Kumar, A.; O'Leary, C.; Dillon, T.; Rolfo, S. Experimental and Computational Investigation of the Emission and Dispersion of Fine Particulate Matter ($PM_{2.5}$) During Domestic Cooking. *Atmosphere* **2024**, *15*, 1517. https://doi.org/10.3390/atmos15121517

Academic Editor: Sunling Gong

Received: 19 November 2024
Revised: 9 December 2024
Accepted: 16 December 2024
Published: 18 December 2024

Copyright: © 2024 by the authors. Licensee MDPI, Basel, Switzerland. This article is an open access article distributed under the terms and conditions of the Creative Commons Attribution (CC BY) license (https://creativecommons.org/licenses/by/4.0/).

1. Introduction

It has long been understood that the air we breathe has an impact on our health, but, for a large part of the 20th century, indoor air quality (IAQ), except in industrial premises, was primarily measured by the metrics of thermal comfort and odour, rather than pollutant concentration [1]. With the advent of ever more densely populated office premises, the problem of the indoor environment was gradually brought to more widespread public attention. A combination of the development of new cleaning products, new synthetic materials for structural and furnishing purposes and the increase in mechanical ventilation systems caused a spike in the reporting of ailments such as asthma, sinusitis and allergic dermatitis by the affected workers. The term "Sick Building Syndrome" was eventually coined in response to this outbreak, to describe all problems caused by a poor indoor environment [1,2]. Since then, progress has been made in the field of IAQ research, but the pace has been far from rapid. While the UK applies the advisory guidelines from several bodies including the World Health Organization (WHO) [3] and the UK Health Security Agency (formerly Public Health England) [4] to the control of indoor air pollutants, these are only guidelines and not legislation. This problem is not limited to the UK as the lack of legally binding regulations for IAQ is a global issue [5]. In the UK, the only legislated

limits for indoor air pollutant exposure are in the workplace, not the home. This exposure is calculated assuming the person exposed is a healthy adult, and is hence irrelevant for a wide demographic of individuals in private housing, including children, the elderly and those with existing health problems [6,7]. Because of this, developing new regulatory standards for indoor air quality has been identified as a key priority in the UK [8]. The recent report from the UK's Department for Environment, Food and Rural Affairs also identified current concentrations of indoor air pollutants in UK homes and their trends over time as being "a major area of uncertainty" due to the dearth of data and, in particular, the lack of multidecadal datasets of the type available for outdoor air quality [6]. That this situation should be improved, and swiftly, is demonstrated by the fact that data from the Global Burden of Disease study indicate that over 90 million global disability-adjusted life years (DALYs) can be attributed to poor indoor air quality [9].

A major contributor to household air pollution (HAP) is $PM_{2.5}$, particulate matter with a diameter of 2.5 µm or less [10]. There is no strict definition for the composition of $PM_{2.5}$; it may be of primarily organic or inorganic composition, or a combination of the two, depending on its origin [11]. This type of particulate matter is fine enough to penetrate the lungs and circulate within the body via the bloodstream, causing chemical and mechanical damage in the process. This makes it a causative or exacerbating factor for both respiratory and cardiovascular diseases [12–15]. Cooking is a key source of $PM_{2.5}$ within households and, as an everyday activity, is responsible for both acute and chronic exposure to $PM_{2.5}$ [16,17]. In the UK, cooking is usually performed using a gas or electric cooker rather than a solid-fuel stove [18]. It could thus be incorrectly assumed that, without a solid-fuel source (which is known to be a high emitter of particles [19]), the contribution of cooking to overall indoor $PM_{2.5}$ concentrations is fairly limited. This is categorically not the case. Local $PM_{2.5}$ concentrations from cooking depend on a wide range of factors, including cooking ingredients and technique, as well as the configuration of the individual kitchen (the variation in these factors being one of the challenges in the characterisation of cooking-related $PM_{2.5}$ pollution in the home). Studies have shown that most forms of cooking give temporary spikes in the concentration of $PM_{2.5}$ in regions close to the cooking source that are orders of magnitude above the WHO-recommended 24 h average concentration of 15 µg m^{-3} [20–23]. Further, global concentrations in the household may remain strongly elevated for 1-10 h after the original emission event, again depending on the type and location of ventilation available [23]. Exposure to $PM_{2.5}$ during cooking procedures is, therefore, a very tangible risk factor for respiratory and cardiovascular disease, even when cleaner forms of fuel are used.

It is evident, therefore, that there is a pressing need to fill the data gap relating to HAP in general and $PM_{2.5}$ pollution from cooking in particular. To do so will require a broad range of techniques. In the Chief Medical Officer for England's 2022 Annual Report, a key recommendation was that a "better understanding of how we can prevent and reduce indoor air pollution" needs to be reached as soon as possible [24]. It further noted that, to be most effective, indoor air quality research must be multi-disciplinary [25]. This is the aim of the current study: to investigate the evolution of $PM_{2.5}$ concentrations in the DOMESTIC kitchen laboratory during stir-frying, using both experimental methods and cutting-edge computational modelling. The layout of DOMESTIC, along with the modelled domain, can be seen in Figure 1. Stir-frying is among the cooking procedures which generate the most $PM_{2.5}$ by mass, due to the amount of oils used in these dishes and the high temperatures at which they are cooked [26,27]. This, coupled with the fact that the stir fry is a cheap and popular dish, makes it an ideal subject for investigation. The computational modelling technique used in this study is Computational Fluid Dynamics (CFD). CFD has a long history of effective use in the modelling of indoor air quality problems in a wide range of settings, including schools, aeroplanes, offices and hospitals, and has most recently been prominent in modelling the dispersion of droplets containing the SARS-CoV-2 virus [28–31]. When modelling particulate matter dispersion using CFD, there are two main approaches which can be taken: the Eulerian–Eulerian approach, in which both the fluid and the solid

phases are modelled as a continuum, and the Eulerian–Lagrangian approach, where the fluid phase is modelled as a continuum and the individual trajectories of the particles are tracked by solving their equations of motion (this is known as Lagrangian Particle Tracking, or LPT) [32]. A full discussion of LPT and its application to CFD modelling can be found in [33,34]. There are benefits to both approaches, but Eulerian–Lagrangian methods are known to perform well in unsteady cases, and provide easier access to data such as mass concentrations [31,35]. For these reasons, the Eulerian–Lagrangian approach was selected for this work. The accuracy of results from CFD simulations is greatly dependent on the fineness of the mesh used to spatially discretise the computational domain, the time step (the temporal increment between computational states) and the choice of model selected for the fluid turbulence [36]. The rapid development of High-Performance Computing (HPC) over the past decade has, however, offered the possibility to develop CFD models which exploit the potential of these new resources. For the current study, both Reynolds-Averaged Navier–Stokes (RANS) and Large Eddy Simulation (LES) turbulence models were trialled to determine their relative performance as a function of the mesh resolution. The experimental results of the study acted as validation data for these models. The usefulness of fully validated numerical models of this type cannot be overemphasised, as they enable the relatively simple testing of multiple scenarios, including ventilation, complementing and extending the capabilities of practical experimentation to both investigate emission events and prescribe mitigation strategies.

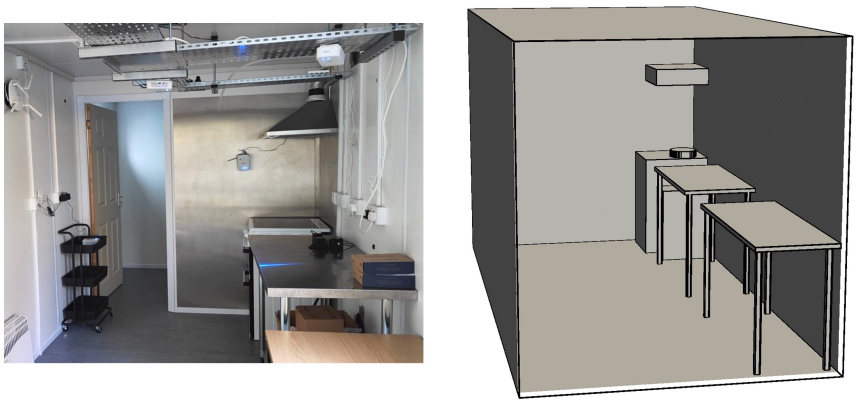

Figure 1. The DOMESTIC kitchen laboratory (**left**) and the modelled domain used for the computational studies (**right**).

2. Materials and Methods

2.1. Validation Experiments: The DOMESTIC Kitchen Laboratory

During February–March 2023, an experimental campaign was undertaken at the Wolfson Atmospheric Chemistry Laboratories at the University of York to investigate emissions from cooking and to obtain verification data for the computational model. The experimental work was conducted in the DOMESTIC kitchen laboratory, which consists of a full-scale kitchen/diner and a bathroom, housed in a heavily insulated crate. This facility was initially based at the University of Chester [37], and was subsequently transferred to its current location in 2022. The kitchen is equipped with an electric cooker—evidence is currently mixed as to whether the use of a gas cooker has a material influence on the mass of $PM_{2.5}$ emitted (see [38,39])—and it was desired that, as far as possible, the only source of $PM_{2.5}$ was the food itself. Gas cookers are also a notable source of nitrogen oxides (NOx) pollution in the home [40], and, though these emissions are not the focus of the current work, this is topic to be investigated in future studies. DOMESTIC can be ventilated using its window or an extractor fan, but, in this set of experiments, the window was kept closed and the extractor fan was not used. DOMESTIC is also equipped with a direct-exhausting cooker hood, but, again, this was not used in the present study as the aim was to investigate an extremely-low-ventilation ("worst-case") scenario first. However, this

will certainly be utilised in future studies looking into mitigation approaches. According to previous measurements taken using acetonitrile tracer releases, the Air Change Rate (ACR) for DOMESTIC under these conditions is 0.77 h^{-1} (standard error 0.064 h^{-1}) [37]. As the focus of the experimental work was the kitchen area, the connecting door between the kitchen and the bathroom was kept closed during the experimentation, making the dimensions of the facility 4.3 × 2.2 × 2.3 m (l × w × ht) (see Figure 2a).

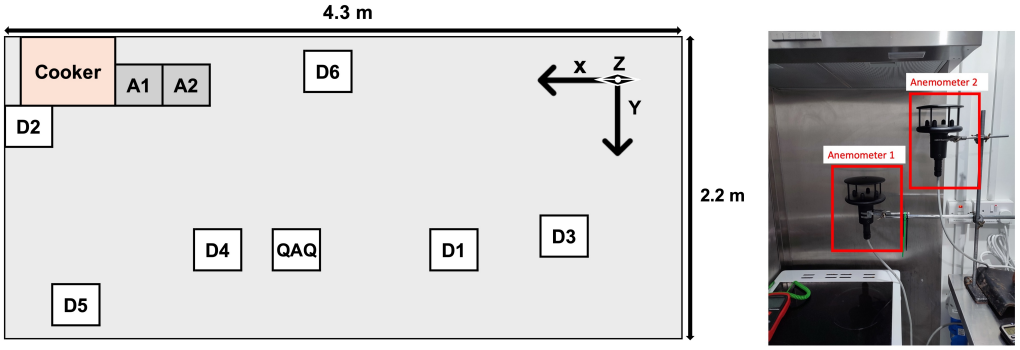

(**a**) (**b**)

Figure 2. (**a**) Layout of DOMESTIC indicating the relative locations of the anemometers (A1 and A2) and QuantAQ (QAQ) and NuWave (D1-6) sensors. PM sensors were placed at approximately head height, with the exception of D5, which was at table height. Arrows indicate the x- and y-direction of the anemometer measurements, with the positive z-direction being towards the reader. (**b**) Close-up of anemometer locations.

2.1.1. Sensors and Instrumentation

Two Gill Instruments WindSonic M ultrasonic 2D anemometers [41] were placed in the vicinity of the cooker to monitor airflow around the cooking source. This type of anemometer is more commonly used outdoors but is robust and has a good time resolution (0.25 s), and anemometers of this brand have been successfully used in similar environments previously [42,43]. The anemometers measured velocity in the x- and y-direction only—these directions are illustrated in Figure 2a—and a close-up of the location of the anemometers is shown in Figure 2b. For the locations of these and all sensors within the DOMESTIC kitchen laboratory, see Figure 2a and Table 1.

Table 1. Locations of anemometers and PM sensors. x, y and z locations are relative to the back right-hand corner of the room, as shown in Figure 2a.

Sensor Abbreviation/Full Title	x Centrepoint (m)	y Centrepoint (m)	z Centrepoint (m)
A1/WindSonic M Anemometer_1	3.55	0.16	1.1
A2/WindSonic M Anemometer_2	3.55	0.16	1.4
D1/NuWave AirSentric WB55 AR10-B-118-A_D1	1.55	1.55	1.92
D2/NuWave AirSentric WB55 AR10-B-118-A_D2	4.28	0.65	1.27
D3/NuWave AirSentric WB55 AR10-B-118-A_D3	0.76	0.81	2.25
D4/NuWave AirSentric WB55 AR10-B-118-A_D4	2.8	1.55	1.92
D5/NuWave AirSentric WB55 AR10-B-118-A_D5	4.08	2	0.74
D6/NuWave AirSentric WB55 AR10-B-118-A_D6	2.34	0.35	1.92
QAQ/QuantAQ MODULAIR-PM	2.5	1.55	1.92

A QuantAQ MODULAIR-PM low-cost sensor (QuantAQ, Somerville, MA, USA) was placed on the exterior of the kitchen laboratory and an identical unit was placed within the kitchen laboratory, for indoor–outdoor comparisons of PM concentrations. These sensors consist of combination of a nephelometer (Plantower PMS5003, Plantower Technology, Nanchang, China) and an optical particle counter (Alphasense OPC-N3, AlphaSense, New

York, NY, USA). The spectra from these are combined to provide PM_1, $PM_{2.5}$ and PM_{10} mass concentrations. The time resolution of these sensors is 1 min, and the sensing range for particulate matter is 0–2000 µg m^{-3} (concentrations above this point may register, but their reliability is not guaranteed) [44]. The QuantAQ sensor was selected as it has performed well in independent tests against high-cost sensors such as the Teledyne API T640 (Teledyne API, San Diego, CA, USA) and the GRIMM 11-D aerosol spectrometer (GRIMM, DURAG Group, Hamburg, Germany), with strong correlations between the sensors, although the QuantAQ showed a tendency to overestimate $PM_{2.5}$ concentrations by around a factor of 1.5–2 during sudden peaks [45]. Considering the differential cost of around GBP 16,000, this was considered to be an acceptable trade-off.

Six low-cost NuWave AirSentric WB55 AR10-B-118-A wireless indoor air quality monitors (AirSentric, Manchester, UK) were chosen and distributed to spatially discretise the domain. These sensors measure CO_2, PM_1, $PM_{2.5}$, PM_{10}, temperature and humidity, with a time resolution of 20 s [46]. These were also compared to the GRIMM in a recent study and showed good correlation but some variability—they were found to be the best of the five low-cost sensors tested in this study in terms of performance [47]. However, a limitation of these sensors is their sensing range for particulate matter, which is 0–1000 µg m^{-3}, potentially below the expected concentrations near the source [46].

2.1.2. Cooking Protocol

A standardised stir-frying protocol was followed, based on the protocol developed in recent studies [37,48,49] in which the weight, freshness and source of the ingredients are tightly controlled, along with the movements of the experimenter during the cooking process. The only alteration across the seven repeats which were performed was that, in three of the repeats, the same weight of chicken was substituted for tofu, to investigate the effect of this ingredient. The full protocols, including ingredient lists, can be found at the STFC Research Data Depository [50]. For each repeat, the ingredients were prepared separately, brought into the kitchen laboratory, placed into a pan heated to 180 °C and cooked for 12 min on the back-right ring of the electric ceramic stove (KDC5422A, Beko, Watford, UK) in a 24 cm Morphy Richards stainless-steel frying pan. Following the 12 min cooking period, the pan was covered with an airtight seal and immediately removed from the kitchen laboratory. The container was then vented for a minimum of 2 h until the background $PM_{2.5}$ concentrations had returned to base level.

2.2. Numerical Models

2.2.1. The Code_Saturne Lagrangian Particle Tracking (LPT) Module

While code_saturne offers the option to include turbulent dispersion in the LPT model, this has historically caused overprediction of particle deposition [29,51], and, during initial tests, this proved to be the case for the current simulations. Therefore, particle turbulent dispersion was omitted here. This should not have a material effect on the accuracy of the results, due to the small size of the particles considered here [31]. It should be noted, however, that pending updates to the particle trajectory algorithm are likely to improve its performance in this area [52]. Thus, when using one-way fluid–particle coupling, the equation for particle position is as follows:

$$dx_{p,i} = U_{p,i}dt$$

where $x_{p,i}$ is the fluid particle displacement over the time step dt and $U_{p,i}$ is the particle velocity. The equation to update particle velocity is as follows:

$$dU_{p,i} = -\frac{1}{\rho}\frac{\partial\langle P\rangle}{\partial x_i}dt - \frac{1}{T_L}(U_i - \langle U_i\rangle)dt + \sqrt{C_0\langle\varepsilon\rangle}dW_i$$

where ρ is the fluid density, P is the fluid pressure, T_L is the Lagrangian timescale of the fluid particle velocities, C_0 is a constant, $\langle\varepsilon\rangle$ is the dissipation rate of the turbulent

kinetic energy and dW_j is a Wiener process, which represents the turbulence-induced random fluctuations. This is the simplified Langevin model [34,51]. The code_saturne LPT module is designed for both structured and unstructured meshes, and the complete numerical approach covering the fluid and particle phases can be described as a hybrid Eulerian–Lagrangian approach, although the authors of the model note that a more accurate description would be a Moment/Probability Density Function hybrid approach [53].

2.2.2. CFD Model of DOMESTIC

A block-structured grid of either c. 40 or c. 170 million cells was generated using the meshing software SALOME, version 9.9.0 [54]. For the solution of the Navier–Stokes (NS) equations in their unsteady, incompressible form, the finite volume solver code_saturne (version 8.0.3) was used [55,56]. Full details of the numerical approach used by this solver can be found in the code_saturne Theory Guide [57]. As, in this case, density variations were expected to be due primarily to natural convection, the Boussinesq approximation was used, in which density variations are represented only via the buoyancy term in the momentum equation [58]. Due to the shortness of duration of the experiment, and the low ACR seen in the kitchen laboratory, no air leakage was included in the model. The convective terms were discretised in space using a centred (second-order accurate) approach, and the Semi-Implicit Method for Pressure-Linked Equations—Consistent (SIMPLEC) algorithm was used for pressure–velocity coupling. A temperature of 11.4 °C was used for the initial temperature of the air, the floor was given an initial temperature of 8.8 °C, the ceiling was given an initial temperature of 11.4 °C and the adiabatic condition was applied to the side walls. The no-slip condition was used for all solid walls. To represent the frying pan, a cylinder was defined in the computational domain, and the surface temperature of this was maintained at 180 °C via a heat source term. To represent the effects of the steam from cooking, an additional momentum source term in the z-direction (directly upwards towards the ceiling) was applied in the region surrounding the frying pan. For the RANS approach, the EBRSM turbulence model [59] with a two-scale wall function model, along with the Daly Harlow method for the turbulent diffusion term, was used. For the LES approach, the Dynamic Smagorinsky [60] and WALE [61] sub-grid-scale models were tested. Turbulent heat fluxes were modelled using the Simple Gradient Diffusion Hypothesis (SGDH). A constant time step of 0.01 s was used for both the 40 and 170 million cell cases, except the 170 million cell WALE case, where a constant time step of 0.005 s was used. For a discussion of the reasoning behind this decision, see Appendix A.

2.2.3. Particle Emission Modelling

Particles with an initial velocity and temperature of the local fluid were injected at the location of the frying pan. Particles were rigid and spherical, with a density of 1.0 g cm^{-3}, representative of a generic organic aerosol [20]. Particle composition was assumed to be homogenous. Following a 2 min tapered increase to represent the increase in the emission rate seen at the start of cooking, the emission rate for $PM_{2.5}$ was held constant at 3.2 mg min^{-1}. This rate was derived from the experimental data and a recent experiment using a similar recipe in which emission rates were calculated [48]. Based on the range of mass concentrations observed by Farmer et al. [20], this rate was subdivided into three categories of particles: those with a diameter of 0.5 ± 0.001 µm, those with a diameter of 1.0 ± 0.001 µm and those with a diameter of 2.5 ± 0.7 µm. The respective emission rates were 0.8, 0.8 and 1.6 mg min^{-1}. Considering the rate of particle emission and the duration of the study, statistical weighting was used to reduce the computational intensity, with each injected computational particle representing approximately 265 actual particles. As the particle flow was relatively dilute in relation to the bulk phase, one-way fluid–particle coupling was used. The stochastic differential equations were integrated using a first-order scheme. To account for dry deposition, on contact with any surface, the particles were assumed to deposit on that surface using the "deposition and elimination" condition available in code_saturne. Particle concentrations were averaged across a 20 cm^3 box

surrounding the midpoint of each sensor. As in the experimental cases, the computational cases were run for 12 min in-simulation time, plus an additional initial minute to allow the frying pan to reach 180 °C. Computations were performed on ARCHER2 and on the Scientific Computing Application Resource for Facilities (SCARF). Postprocessing of results was carried out using ParaView [62] for 3D images and Matplotlib for graphical images.

3. Results and Discussion

3.1. Indoor–Outdoor $PM_{2.5}$ Ratios During Experimentation

Tracking the indoor and outdoor $PM_{2.5}$ data from the QuantAQ sensors demonstrated that the outdoor $PM_{2.5}$ concentrations were not elevated during the cooking period. This confirmed that outdoor sources made a minimal contribution to the indoor concentrations, meaning that the observed elevated indoor concentrations can be reasonably attributed to the indoor source (see Figure 3).

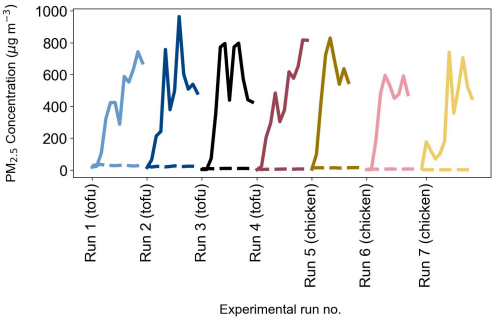

Figure 3. QuantAQ indoor–outdoor ratios during the 12 min stir-frying experiments in DOMESTIC. Dotted lines indicate outdoor readings, solid lines indoor readings.

3.2. NuWave $PM_{2.5}$ Data

As Figure 4 shows, although rigorous standardisation was applied across all experimental runs, there was noticeable variation in the $PM_{2.5}$ readings between certain runs, particularly at sensor D2 (Figure 4b), the sensor closest to the source. This was expected, as previous tests demonstrated that the stir-frying process is not only one of the higher-emitting cooking processes, but also gives considerably variable results [63]. One reason for this is likely the technique required, which involves rapidly shaking the pan at intervals. The total mass of particles emitted is, therefore, at least in part, dependent on experimenter technique. The volume of steam generated can also have an impact on sensor readings. In the experimental cooks, humidity within the kitchen laboratory was often high, over 60% Relative Humidity (RH) even before cooking commenced, and the stir-frying process generated a large volume of steam. RH readings at the end of the experimental period were, with the exception of at the D5 sensor, regularly between 80 and 90%. RH readings at D2 showed rapid, broad fluctuations, indicating that clouds of steam likely passed the sensor (all humidity data for all runs can be found at the STFC Research Data Depository [50]). Dependent on the hydrophobicity of the particles, particle-bound water can distort low-cost sensor readings by increasing light scattering [63,64] and this may have acted to artificially inflate the readings of mass concentrations of $PM_{2.5}$ at this sensor. The measured mode particle diameters were consistently the largest at this sensor (see Figure A3), which correlates with the higher $PM_{2.5}$ concentrations seen at this sensor. This may, again, indicate that particle size is being inflated by local humidity. The variation between the runs does not seem to correlate with differences in the cooking material. For example, the readings for D1 Run 7 (using chicken as the protein component of the stir fry) are comparable to the readings for D1 Run 4 (using tofu) (see Figure 4a), with a similar pattern being observable at the D3 sensor (see Figure 4c). For this reason, all experimental runs were included in the calculation of the mean concentration used for comparison with the simulated results. Note that, for Runs 2, 3 and 4, the sensor D5 was moved to floor

level to test $PM_{2.5}$ concentrations at this level (see Figure 4e). These readings have therefore been excluded from the calculation of mean concentrations at this sensor used later in these results. In terms of the concentrations observed at each sensor, it is clear that there was a noticeable difference in the readings dependent on the placement of the sensor. The D5 sensor, which was placed either at table height or on the floor, showed the lowest readings (with a maximum of around 120 µg m^{-3}), while D3, the ceiling sensor closest to the kitchen laboratory exit (and furthest from the cooking source), had the highest readings after D2, with peaks in concentration of up to 5000 µg m^{-3}. This is likely because it was situated in the corner of the room, which allowed clouds of particle-laden air to gather and stagnate rather than dispersing as they did for the more centrally positioned sensors.

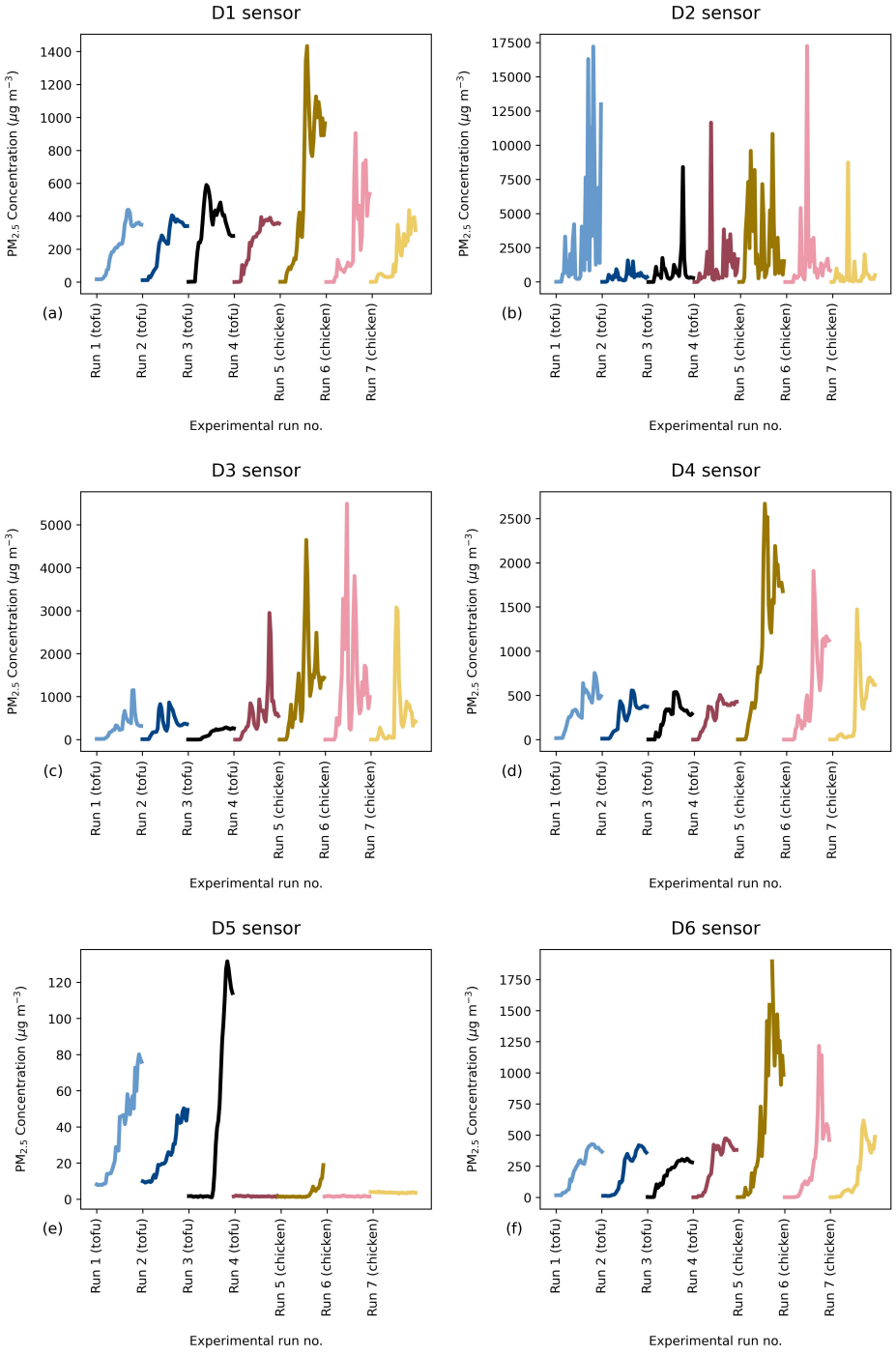

Figure 4. NuWave readings at sensors D1–6 (**a**–**f**) for the seven 12 min stir-frying experiments.

The guaranteed sensing range of the NuWave sensors should be borne in mind when interpreting these peaks; however, even making an allowance for a reduction in accuracy above concentrations of 1000 µg m^{-3}, it is clear that the 12 min stir fry increased $PM_{2.5}$ within the breathing zone of the kitchen laboratory by several orders of magnitude. This is further borne out by the results from the QuantAQ sensor, positioned in the centre of the kitchen laboratory, which showed rather more standardised readings across the seven runs, with peaks of around 800 µg m^{-3} (see Figure 3). These concentrations align with those observed by O'Leary et al. for a similar cook [48], albeit at a greater ACR (around 3 h^{-1} vs. 0.77 h^{-1}). They are, however, considerably higher than the maximum of 400 µg m^{-3} reported by Farmer et al. in the HOMEChem study [20] when stir-frying a similar recipe. In the latter study, an HVAC system was used, which would have mitigated the indoor concentration levels. As most interior room doors were left open in the 250 m^3 UTest house during the HOMEChem cooking experiments, the mixing volume in the HOMEChem study was also much greater than that in DOMESTIC, which, again, likely reduced the observed concentrations. The difference seen in the DOMESTIC $PM_{2.5}$ readings dependent on sensor position in this study indicates the importance of using a multi-point sensor approach when assessing the impact of an indoor pollutant source on the surrounding environment. Clearly there is the potential for considerable spatial variation in concentrations even in a relatively small space. Of course, in a real-life kitchen, there is likely to be considerably more mixing, due to additional human movement and ventilation sources. However, even accounting for this, the existence of localised zones of higher $PM_{2.5}$ concentration should be considered.

3.3. Mode Particle Diameter and Contribution of PM_1 to $PM_{2.5}$ Mass Concentrations

Number size distributions—that is, the contribution of particles of various diameters to the total particle count—are of interest when conducting air quality investigations. This is because particles in the accumulation mode, around 0.01–1 µm diameter, remain airborne and stable for considerably longer than those that are either smaller (which tend to agglomerate to accumulation mode size) or larger (which normally deposit at a faster rate, dependent on respective densities) [65]. This then has implications for longer-term exposure. Figure A3 shows the mode particle diameter measured by the NuWave sensors during the seven stir fry cooking experiments. This was around 0.575 µm, that is, in the accumulation mode. The mode diameter increased over the course of the experiment, peaking for all sensors except D5 soon after the chicken/tofu was added to the pan (with the highest reading being at the D2 sensor, around 1.1 µm, before decreasing again). It is likely that the addition of the cold protein source to the hot oil generated the rapid production of larger particles via the ejection of oil droplets from the pan, and this effect was then reduced once the mixed vegetables, noodles, etc., were added. The full data on particle counts for $PM_{0.5}$, PM_1, $PM_{2.5}$, PM_4, and PM_{10} for all experimental runs can be found at the STFC Research Data Depository [50]. In terms of the relative contribution of PM_1 to $PM_{2.5}$ concentrations, there is some disagreement between the NuWave and QuantAQ sensors. According to the NuWave readings (except for D2, the sensor closest to the source), the majority of the mass of $PM_{2.5}$ was made up of particles of under 1.0 µm in diameter, while the QuantAQ sensor indicated that around 50% of the mass concentration was made up of PM_1 (see Figure A4). The QuantAQ sensor was relatively near NuWave sensors D1 and D4, and along the same plane in the kitchen laboratory, so it seems unlikely that this was a regional variation. While the NuWave readings are in the majority, the QuantAQ ratios agree with Farmer, 2019 [20], and, hence, for the modelling, these are the data that informed the particle size range chosen for the computational model. The disparity does, however, illustrate another challenge of using low-cost sensors, which is that calibration processes may vary quite considerably, and the particles used for calibration are often chemically and physically dissimilar to the type of particulate matter commonly generated by cooking [48]. It is likely that at least part of the disparity seen here between the sensor types can be attributed to different calibration protocols.

3.4. Experimental Velocities

The experimentally measured velocities for both anemometers in all directions were low, with the maximum range being around $\pm 0.3\,\mathrm{m\,s^{-1}}$. This was as expected for this environment without natural or artificial ventilation, as the air currents were driven by human movement and the heat from the cooking experiment only. As Figure 5 shows, there was a perceptible increase in the velocities registered at the anemometers as soon as a member of the experimental team entered DOMESTIC. The example given is for Run 1, but the same pattern was observed for all experimental runs. This shows that, despite the low measurements, the anemometers were registering actual changes in the local velocities rather than these readings representing instrumental noise. One challenge with these data is that the contribution of human movement to the overall observed velocities cannot be easily isolated. As Figure 5 shows, there was an increase in the velocity measurements just before and immediately after the pan reached 180 °C. However, this coincided with the experimenter stepping closer to the anemometers to begin cooking, and so the heat source may not have been the only cause of this increase. As discussed below, this added some difficulties in the comparison with the computational model.

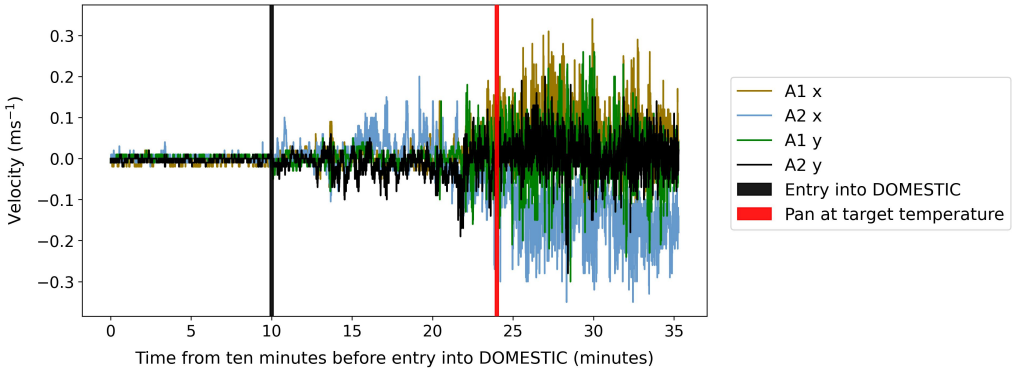

Figure 5. WindSonic M readings for Run 1 (tofu), showing the 10 min period before DOMESTIC was entered and the experimental period.

3.5. Experimental vs. Simulated Velocities

Figure 6 shows the differences between the experimental and computational velocities over the course of the experiment. The 170 million cell WALE results are presented here, as these are representative of the results from all six cases, which were relatively homogeneous. For anemometer 1, the x-direction computational velocities showed a difference of around $\pm 0.05\,\mathrm{m\,s^{-1}}$ for the first 4 min, after which the experimental results became progressively more negative than the computational results (Figure 6a). In the y-direction, the difference was around $\pm 0.05\,\mathrm{m\,s^{-1}}$ with occasional peaks to $0.1\,\mathrm{m\,s^{-1}}$(Figure 6b). The largest differences (up to $-0.3\,\mathrm{m\,s^{-1}}$) were seen in the x-direction velocities for anemometer 2. Here, the computational model predicted positive velocities, while those measured experimentally were uniformly negative (see Figure 6c). As Figure 7a shows, the computational model did predict regions of negative x velocities of up to $-0.25\,\mathrm{m\,s^{-1}}$ around the frying pan, but not at the specific point at which the anemometer 2 monitoring point was set. The y-direction velocities for anemometer 2 showed a range of difference around $\pm 0.12\,\mathrm{m\,s^{-1}}$, although most differences were around $\pm 0.05\,\mathrm{m\,s^{-1}}$ (Figure 6d). Figure 7b visualises these velocities across a plane intersecting the pan. These discrepancies could stem from a variety of sources. Experimenter movement may have been a substantial contributing factor to the experimental velocities, and this movement did not appear in the model. The stir-frying process also generated a large amount of steam. In the computational model, some of the effects of this were represented by a momentum source term in the z-direction, but this is still a simplification of the actual effects. Lastly, the structure of WindSonic M anemometers is fairly bulky, and there is a risk that this structure may distort the fluid velocities around

them. This is an issue with using these larger anemometers, where there is a trade-off between the increased sensitivity that they provide and their increased size.

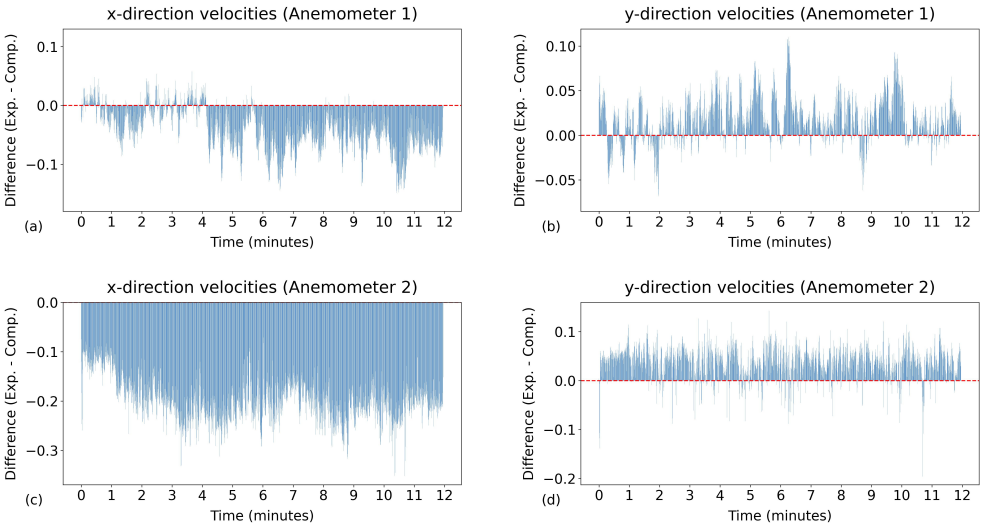

Figure 6. Differences between the mean experimental x and y velocities at anemometers 1 and 2 and the velocities predicted by the WALE 170 million cell mesh model (Exp. = experimental, Comp. = computational). As the experimental velocities oscillated widely, velocities have been averaged over 1-s intervals in order to better visualise trends.

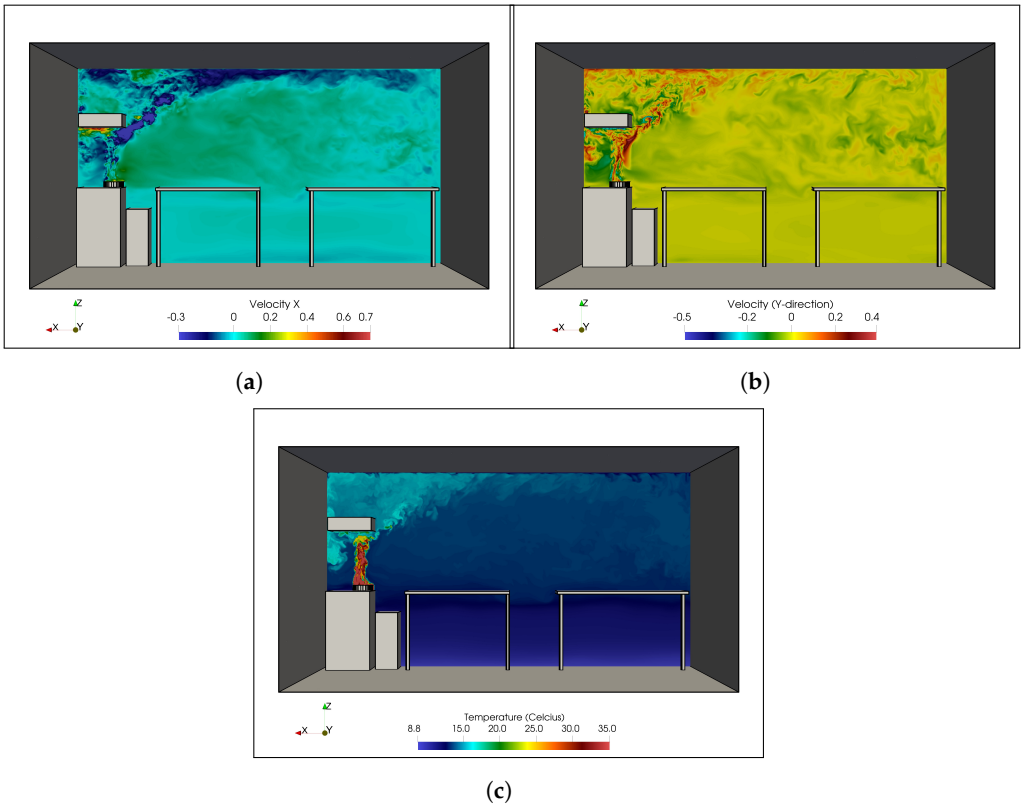

Figure 7. (**a**) X and (**b**) Y velocities across a plane intersecting with the frying pan within the DOMESTIC model. (**c**) Temperatures across a plane intersecting with the frying pan within the DOMESTIC model. All images are from the 170 million cell WALE case, and the results shown are from the final minute of the 12 min cooking period.

3.6. Experimental vs. Simulated Temperatures

Despite DOMESTIC having heavy insulation, due to the wide external fluctuations between temperatures on different experimental days, it was not possible to standardise the starting temperatures within the kitchen laboratory between each run. In every case, however, a steady increase in temperature was observed, making a comparison of the ΔT for each sensor and run feasible. As Figure 8 shows, certain trends are visible. As expected, the sensor closest to the heat source, D2, consistently registered the highest increase in temperature, normally of approximately 1.75 °C. Similarly, the sensor placed on the table (D5) consistently registered the lowest increase in temperature, of under 0.3 °C. The other sensors, all of which were hung from a gantry on the ceiling, showed reasonably similar ΔT results, which is encouraging as it indicates the repeatability, and thus the reliability, of the readings. For the 170M computational cases, the Dynamic Smagorinsky and WALE cases both gave a similar performance, with a temperature increase at all simulated monitoring points that overestimated the observed experimental results—except for at D2, the closest sensor to the pan, where a good agreement was seen. A slightly lower overprediction was seen for the EBRSM cases for all monitoring points except D5. One cause of these overpredictions is likely that the heat-damping effect of adding ingredients to the pan was not represented in the model, which assumed that the pan temperature remained constant at 180 °C. Examining the simulated temperature distributions in the wider domain, they appear feasible, with a typical thermal plume above the heat source and a gradual warming of the circulating air which does not, at the end of the 12 min, reach the lower levels of the room (see Figure 7c).

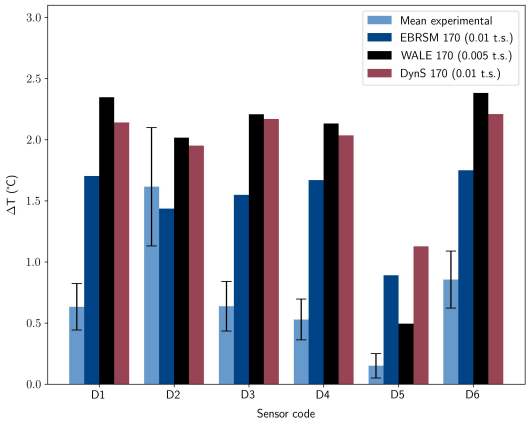

Figure 8. Comparison of mean experimental ΔT with those predicted by the Dynamic Smagorinsky, WALE and EBRSM 170 million cell mesh models (t. s. = time step).

3.7. $PM_{2.5}$ Simulated Results

Particle dispersion progressed as expected in the simulations, with a high-concentration region forming directly around the cooking zone and spreading outwards through the breathing zone over the 12 min cooking period (see Figure 9). For the 40M cell meshes (see Figure 10), both LES cases showed a trend of underestimating $PM_{2.5}$ concentrations, except at the D5 sensor, where the lowest experimental concentrations were observed; here concentrations are, instead, overestimated, as shown in Figure 10e. It must be borne in mind, however, that this is a comparison with a mean concentration from the experimental results. These had a fairly wide range, with final concentrations of over 120 $\mu g\,m^{-3}$ observed for one of the tofu cooks (see Figure 4e). Higher concentrations at this point were, therefore, evidently possible. The EBRSM 40M cell case seriously overpredicted the results (up to triple the experimental readings) at all sensors except the D2 sensor, which, as for the LES cases, was generally underestimated.

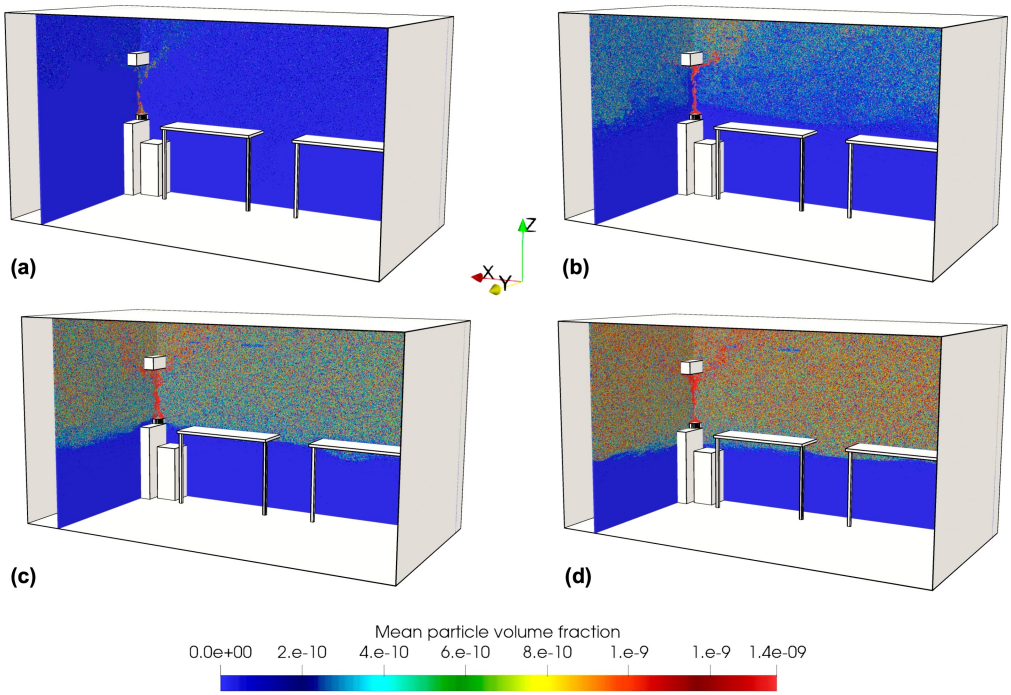

Figure 9. Particle dispersion across two planes in the kitchen laboratory after (**a**) 1 min, (**b**) 4 min, (**c**) 8 min and (**d**) 12 min. Results from the 170 million cell WALE case.

Increasing the mesh resolution to 170M cells generally improved the fit to the experimental results. This was expected as (for LES) mesh refinement not only improves the accuracy of the physics of the fluid flow via better resolution of the large eddies, but also improves the accuracy of particle deposition mechanics [66,67]. The connection between mesh resolution and accuracy is more complex for the RANS/EBRSM approach, but, again, it should still improve particle deposition mechanics. Some overestimations were observed, particularly at D1 and D6 (Figure 11a,f), and the overestimations at D5 seen in the 40 million cell cases were also apparent (see Figure 11e). Readings at D2 were also still underestimated (Figure 11b) although this underestimation decreased for the LES cases. All cases demonstrated a relatively linear increase in $PM_{2.5}$ concentrations at all sensors except D5. This is in contrast to the experimental results, which showed specific peaks, most especially at the point at which the noodles were added to pan and cooked, between minutes 6.5 and 9.5. The steady emission rate assumption used in the model appears to be insufficient to represent the experimental emission rates, which apparently varied significantly, and not necessarily predictably (judging from the individual experimental results seen in Figure 4). The model emission rate was based on the work of O'Leary et al. [48], who, using six repeats, found the mean emission rate for a similar dish that ranged between 2.3 and 4.2 mg min^{-1} depending on the experimental run. It is likely that the use of a variable emission rate within the model would more accurately capture the evolution of concentrations, although establishing the appropriate timing and scale of these variations in experimental conditions would be challenging due to the sheer intrinsic variability of such experiments. In contrast, at sensor D2 (Figure 11b), while the 170 million cell cases showed higher concentrations at this sensor than the 40M cases, they were still, at the majority of points, many times lower than the experimental results. As discussed above, it is possible that the $PM_{2.5}$ concentration readings at the D2 sensor were distorted by the steam generated during cooking, due to the proximity of this sensor to the cooking source. The lower concentrations observed in the simulations are likely due to a combination of this fact and the need for the gusting steam present in the experimental conditions to be better represented in the model. In addition to a more in-depth consideration of the variability of the source emission rate, the incorporation of non-spherical particles, and the exploration of

the potential impact of particle coagulation, is also recommended for future research. Once reliable results can be produced in sealed conditions, the model could then be expanded to include ventilation scenarios, to investigate the most efficient mitigation strategies to protect householders during cooking.

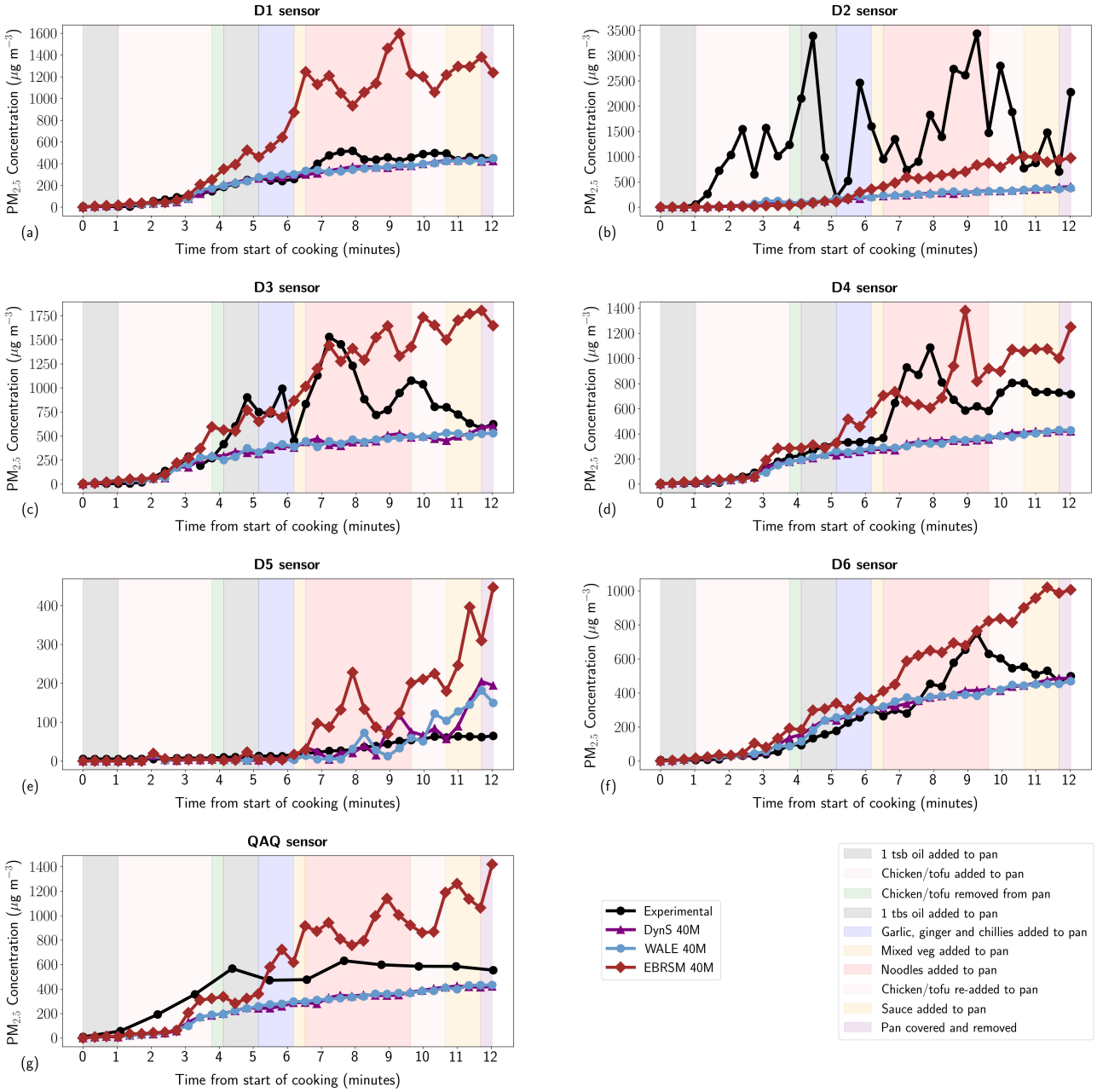

Figure 10. Results for the 40M Dynamic Smagorinsky, WALE and EBRSM cases for $PM_{2.5}$ concentrations during cooking compared with the experimental results. (Note that concentration data were collected every 50 iterations, but have been smoothed to match the frequency of the NuWave readings).

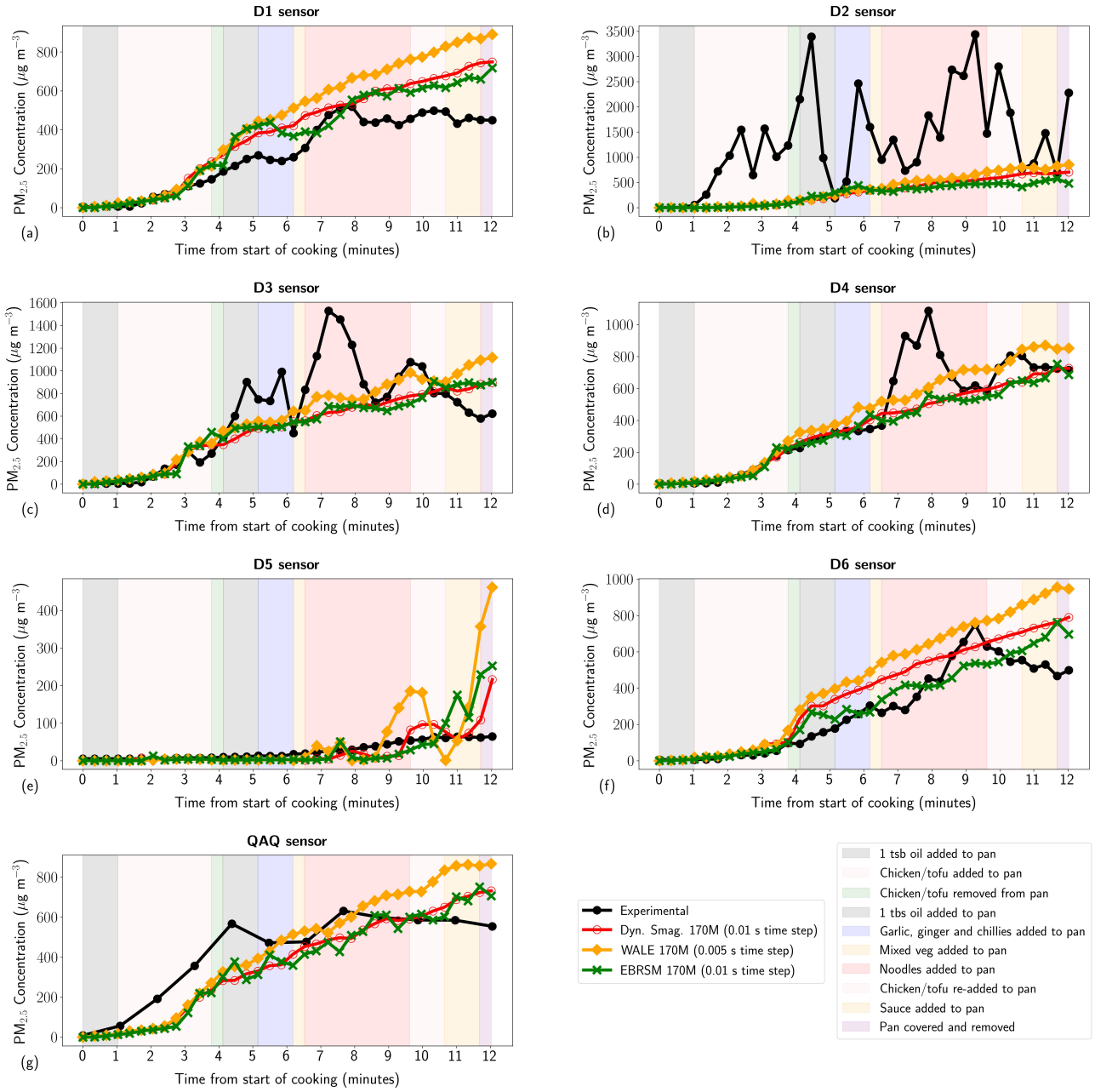

Figure 11. Mean experimental results compared against simulated results from 170M meshes for $PM_{2.5}$ concentrations during experiments. (Note that concentration data were collected every 50 iterations, but have been smoothed to match the frequency of the NuWave readings).

4. Conclusions

The experimental results demonstrated the speed at which $PM_{2.5}$ mass concentrations can rise during this kind of cooking in unventilated areas, with concentrations at certain points reaching nearly 100 times the WHO-recommended 24 h average maximum in under 8 min. This indicates both the importance of appropriate ventilation even for short episodes of cooking and that multi-point monitoring for $PM_{2.5}$ is key for assessing exposure risk. The CFD models showed some agreement with experimental results, but discrepancies in key variables were observable in both the RANS and LES cases. It was evident that results were sensitive to both the fineness of the mesh and the time step relative to the mesh size, with the EBRSM case being apparently the most vulnerable to the influence of these factors. Going forward, the impact of temperature damping, steam and emission rate variability should be investigated, and the addition of particle turbulent dispersion considered.

Author Contributions: Conceptualisation, T.D. and S.R.; methodology, H.J., C.O. and A.K.; software, H.J. and S.R.; validation, H.J.; formal analysis, H.J., C.O. and A.K.; investigation, H.J., C.O. and A.K.; resources, T.D. and S.R.; data curation, H.J.; writing—original draft preparation, H.J.; writing—review and editing, C.O., A.K., T.D. and S.R.; visualisation, H.J.; supervision, T.D. and S.R.; project administration, T.D. and S.R.; funding acquisition, T.D. and S.R. All authors have read and agreed to the published version of the manuscript.

Funding: This work was supported by the STFC Air Quality Network, grant number ST/S005366/1. Compute time on ARCHER2 was provided via an Engineering and Physical Sciences Research Council (EPSRC) "Access to High Performance Computing" grant. The design and construction of the DOMESTIC container was supported by the EPSRC, grant number EP/T014490/1. C.O. was supported by the EPSRC IMPeCCABLE EP/T014792/1 project, and A.K. was supported by the NERC INGENIOUS NE/W002256/1 project. For the purpose of open access, the authors have applied a Creative Commons Attribution (CC BY) licence to any Author Accepted Manuscript version arising.

Institutional Review Board Statement: Not applicable.

Informed Consent Statement: Not applicable.

Data Availability Statement: The dataset supporting this paper is openly available from eData, the STFC Research Data repository at https://doi.org/10.5286/edata/934.

Acknowledgments: Many thanks to the team at EDF R&D for their technical support during the course of this project.

Conflicts of Interest: The authors declare no conflicts of interest. The funders had no role in the design of the study; in the collection, analysis or interpretation of data; in the writing of the manuscript; or in the decision to publish the results.

Appendix A

There were two main criteria for the time step selection. Firstly, that the Courant number (which represents the transport of information across a cell per unit time) remained below one. This prevents information being propagated across multiple cells per time step, causing numerical inaccuracies [68]. Secondly, that the selected time step gave reasonable convergence on the computational data. For the LES 40 million cell cases, there was good enough convergence between the $PM_{2.5}$ data using a 0.02 s time step and a 0.01 s time step to justify using the 0.02 s time step (see Figure A1). However, the EBRSM $PM_{2.5}$ concentration readings were extremely different between the 0.02 s and 0.01 s time step cases. Less discrepancy was seen between the 0.01 and 0.005 s EBRSM cases, but there were still large differences at certain points, of up to around 550 $\mu g\,cm^{-3}$ (see Figure A1). Reducing the time step further would have considerably increased the computational requirement and, for this reason, it was decided that a 0.01 s time step (while is likely unnecessarily low for the LES cases) gave a better indication of the trend in the EBRSM case. For the 170 million cell cases reasonable convergence was seen for the WALE case between the 0.01 and 0.005 s time steps (see Figure A2), with maximum differences in $PM_{2.5}$ concentrations of up to 125 $\mu g\,cm^{-3}$ excepting at sensor D3, where differences of up to around 140 $\mu g\,cm^{-3}$ were seen (see Figure A2. Given the computational intensity of the lower time step, it was decided to use the larger time step for both the Dynamic Smagorinsky and the EBRSM 170 million cell cases. However, it would be interesting to investigate in the future if the EBRSM 170 million cell case is more sensitive to time step reduction than the equivalent WALE case.

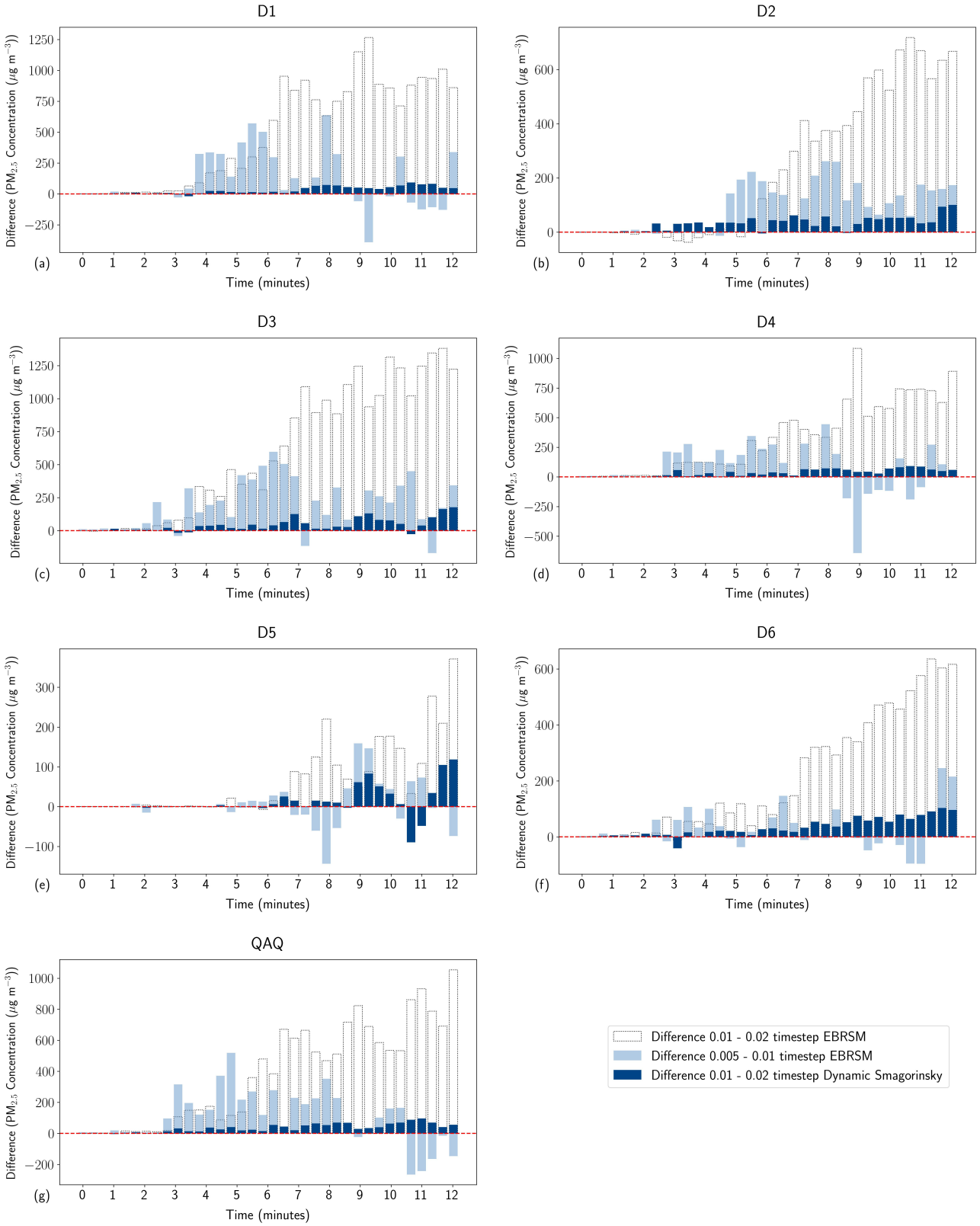

Figure A1. Comparisons between computational results using different sizes of time steps for the 40 million cell mesh.

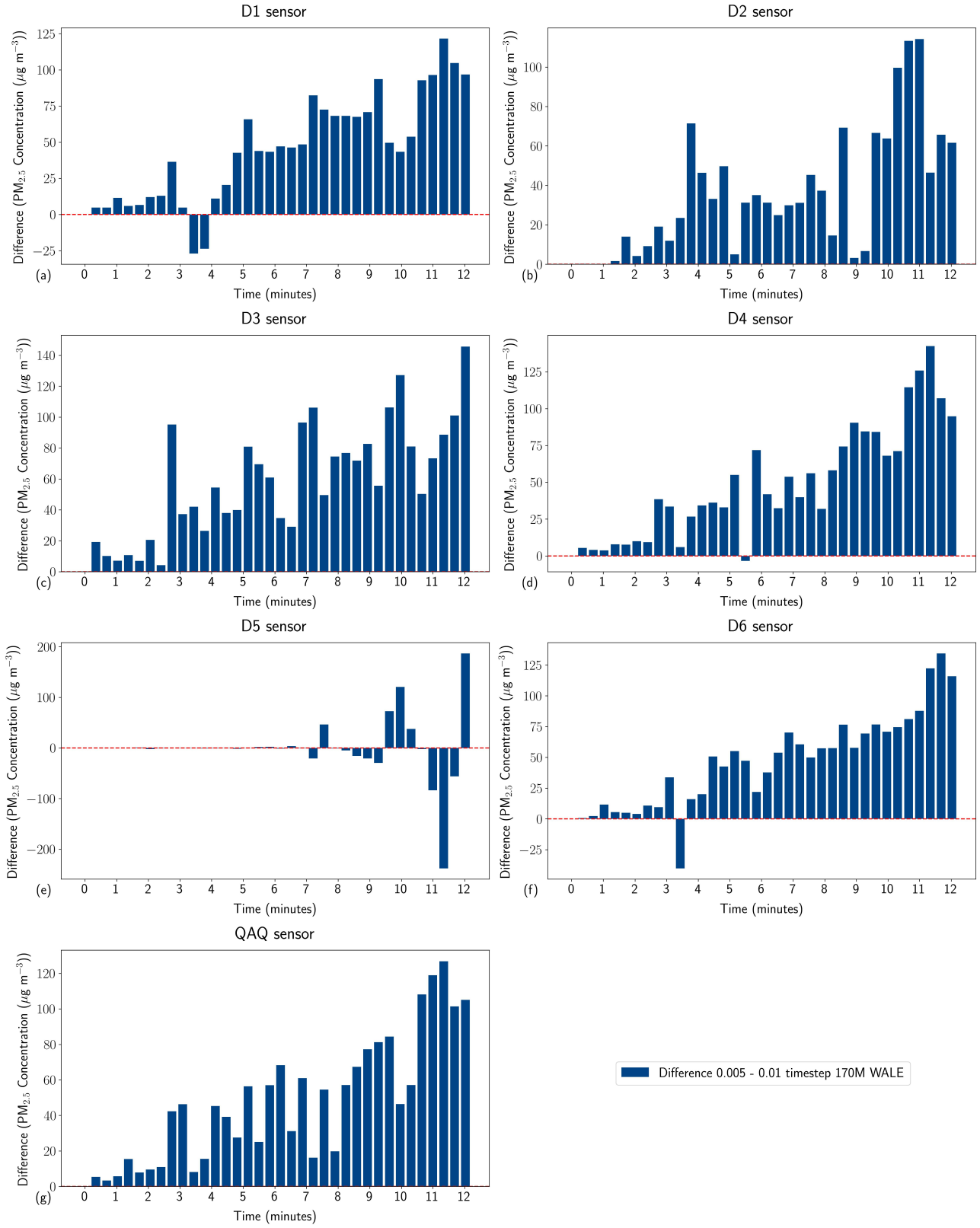

Figure A2. Comparisons between the results for the 0.01 and 0.005 s time step cases for the WALE 170 million cell case.

Appendix B

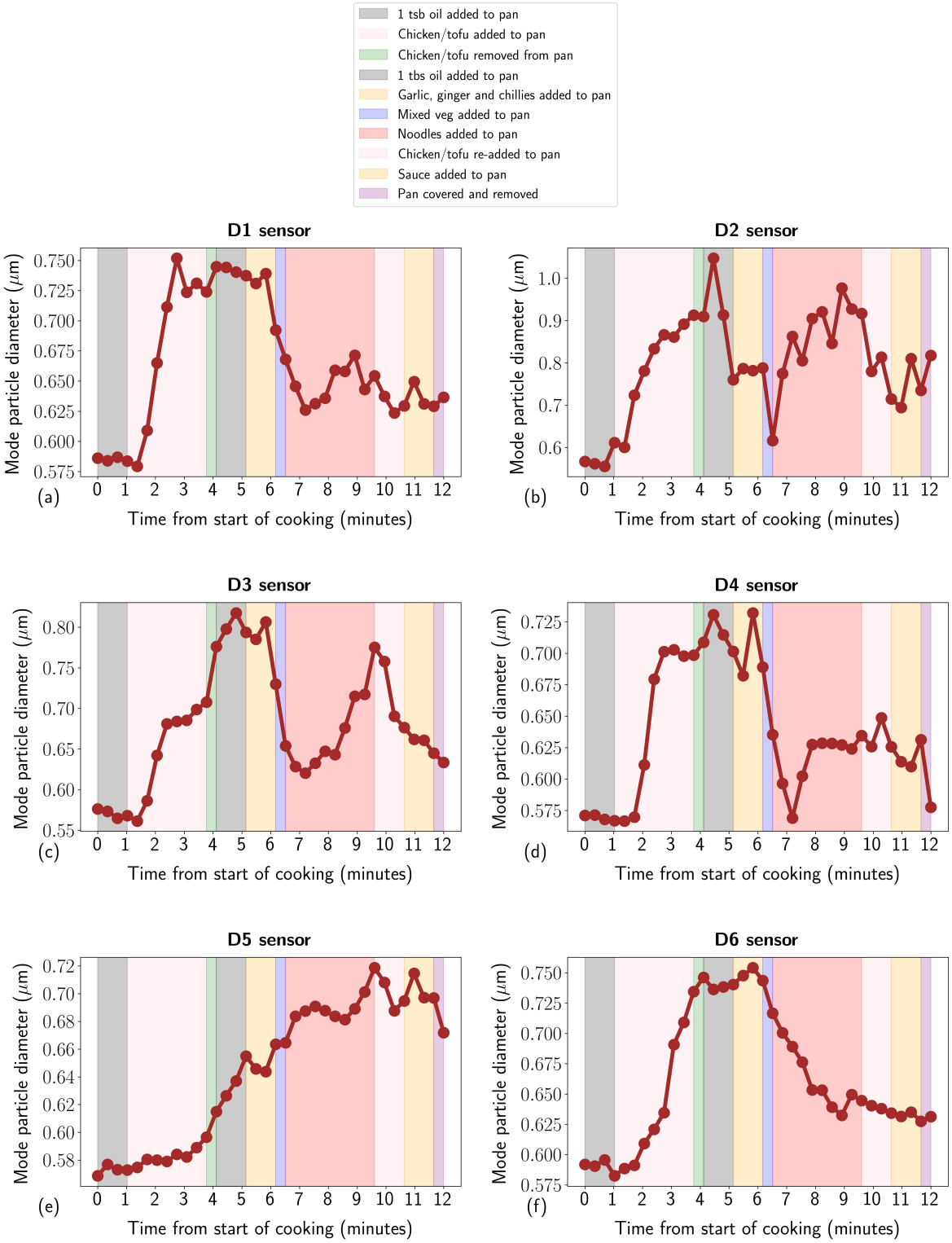

Figure A3. The mode particle diameter across the duration of the stir fry (averaged across the seven runs), as measured at the NuWave sensors.

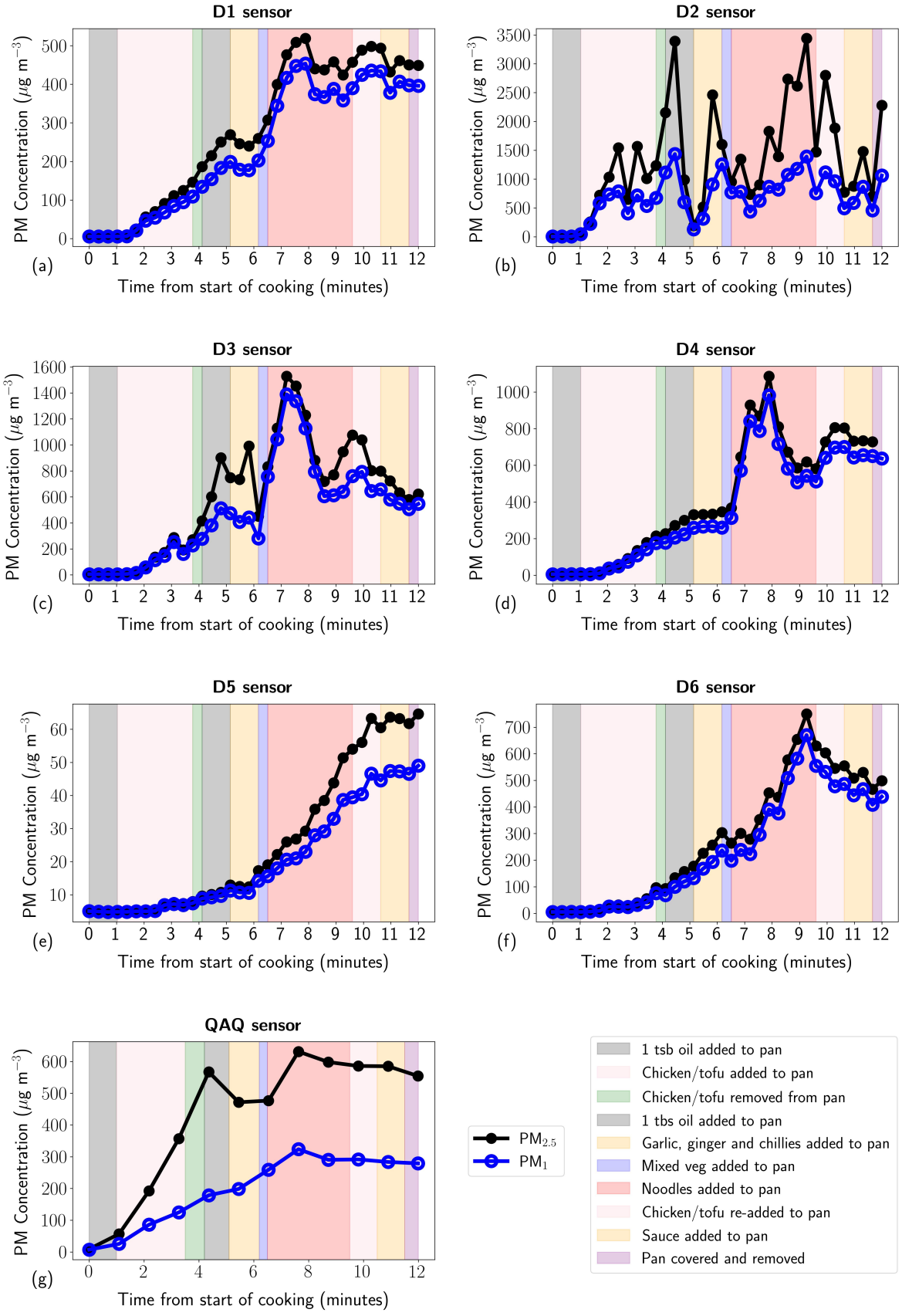

Figure A4. Mean NuWave and QuantAQ $PM_{2.5}$ and PM_1 readings over the course of a 12 min stir fry experiment.

References

1. Sundell, J. On the history of indoor air quality and health. *Indoor Air* **2004**, *14*, 51–58. [CrossRef] [PubMed]
2. Redlich, C.A.; Sparer, J.; Cullen, M.R. Sick-building syndrome. *Lancet* **1997**, *349*, 1013–1016. [CrossRef] [PubMed]
3. Pérez Velasco, R.; Jarosińska, D. Update of the WHO global air quality guidelines: Systematic reviews—An introduction. *Environ. Int.* **2022**, *170*, 107556. [CrossRef] [PubMed]
4. Public Health England. Air Quality: UK Guidelines for Volatile Organic Compounds in Indoor Spaces. 2019. Available online: https://assets.publishing.service.gov.uk/media/5d7a2912ed915d522e4164a5/VO__statement_Final_12092019_CS__1_.pdf (accessed on 15 November 2024).
5. Dimitroulopoulou, S.; Dudzińska, M.R.; Gunnarsen, L.; Hägerhed, L.; Maula, H.; Singh, R.; Toyinbo, O.; Haverinen-Shaughnessy, U. Indoor air quality guidelines from across the world: An appraisal considering energy saving, health, productivity, and comfort. *Environ. Int.* **2023**, *178*, 108127. [CrossRef]
6. DEFRA Air Quality Expert Group. Indoor Air Quality. 2022. Available online: https://uk-air.defra.gov.uk/assets/documents/reports/cat09/2211011000_15062022_Indoor_Air_Quality_Report_Final.pdf (accessed on 15 November 2024).
7. Lewis, A.C.; Moller, S.J. How Air Pollution Is Changing. In *Chief Medical Officer's Annual Report 2022: Air Pollution*; 2022; Chapter 3, pp. 44–71. Available online: https://assets.publishing.service.gov.uk/government/uploads/system/uploads/attachment_data/file/1121614/chief-medical-officers-annual-report-2022-air-pollution.pdf (accessed on 15 November 2024).
8. NICE. Indoor Air Quality at Home: NICE Guideline [NG149]. 2020. Available online: https://www.nice.org.uk/guidance/ng149 (accessed on 15 November 2024).
9. Bennitt, F.; Wozniak, S.; Causey, K.; Burkart, K.; Brauer, M.; Kumar, M.; Ibitoye, S.E. Estimating disease burden attributable to household air pollution: New methods within the Global Burden of Disease Study. *Lancet Glob. Health* **2021**, *9*, S18. [CrossRef]
10. Patel, S.; Sankhyan, S.; Boedicker, E.K.; DeCarlo, P.F.; Farmer, D.K.; Goldstein, A.H.; Katz, E.F.; Nazaroff, W.W.; Tian, Y.; Vanhanen, J.; et al. Indoor particulate matter during HOMEChem: Concentrations, size distributions, and exposures. *Envir. Sci. Tech.* **2020**, *54*, 7107–7116. [CrossRef]
11. Tsigaridis, K.; Krol, M.; Dentener, F.J.; Balkanski, Y.; Lathière, J.; Metzger, S.; Hauglustaine, D.A.; Kanakidou, M. Change in global aerosol composition since preindustrial times. *Atmos. Chem. Phys.* **2006**, *6*, 5143–5162. [CrossRef]
12. Chen, J.; Hoek, G. Long-term exposure to PM and all-cause and cause-specific mortality: A systematic review and meta-analysis. *Environ. Int.* **2020**, *143*, 105974. [CrossRef]
13. van Nunen, E.; Hoek, G.; Tsai, M.Y.; Probst-Hensch, N.; Imboden, M.; Jeong, A.; Naccarati, A.; Tarallo, S.; Raffaele, D.; Nieuwenhuijsen, M.; et al. Short-term personal and outdoor exposure to ultrafine and fine particulate air pollution in association with blood pressure and lung function in healthy adults. *Environ. Res.* **2021**, *194*, 110579. [CrossRef]
14. Thangavel, P.; Park, D.; Lee, Y.C. Recent insights into particulate matter (PM2.5)-mediated toxicity in humans: An overview. *Int. J. Environ. Res. Public Health* **2022**, *19*, 7511. [CrossRef]
15. Local Burden of Disease Air Pollution Collaborators. Mapping development and health effects of cooking with solid fuels in low-income and middle-income countries, 2000-18: A geospatial modelling study. *Lancet Glob. Health* **2022**, *10*, e1395–e1411. [CrossRef] [PubMed]
16. He, C.; Morawska, L.; Hitchins, J.; Gilbert, D. Contribution from indoor sources to particle number and mass concentrations in residential houses. *Atmos. Environ.* **2004**, *38*, 3405–3415. [CrossRef]
17. Brunekreef, B.; Janssen, N.; Hartog, J.; Oldenwening, M.; Meliefste, K.; Hoek, G.; Lanki, T.; Timonen, K.; Vallius, M.; Pekkanen, J.; et al. Personal, Indoor, and Outdoor Exposures to PM2.5 and its Components for Groups of Cardiovascular Patients in Amsterdam and Helsinki. *Res. Rep. (Health Eff. Inst.)* **2005**, *127*, 1–70; discussion 71.
18. Department for Business, Energy & Industrial Strategy. UK Guidelines for Volatile Organic Compounds in Indoor Spaces. 2021. Available online: https://assets.publishing.service.gov.uk/media/61449c3cd3bf7f05b2ac20a4/efus-light-appliances-smart-tech.pdf (accessed on 15 November 2024).
19. Leavey, A.; Patel, S.; Martinez, R.; Mitroo, D.; Fortenberry, C.; Walker, M.; Williams, B.; Biswas, P. Organic and inorganic speciation of particulate matter formed during different combustion phases in an improved cookstove. *Environ. Res.* **2017**, *158*, 33–42. [CrossRef] [PubMed]
20. Farmer, D.K.; Vance, M.E.; Abbatt, J.P.D.; Abeleira, A.; Alves, M.R.; Arata, C.; Boedicker, E.; Bourne, S.; Cardoso-Saldaña, F.; Corsi, R.; et al. Overview of HOMEChem: House Observations of Microbial and Environmental Chemistry. *Environ. Sci. Process. Impacts* **2019**, *21*, 1280–1300. [CrossRef]
21. Tang, R.; Pfrang, C. Indoor particulate matter (PM) from cooking in UK students' studio flats and associated intervention strategies: Evaluation of cooking methods, PM concentrations and personal exposures using low-cost sensors. *Environ. Sci. Atmos.* **2023**, *3*, 537–551. [CrossRef]
22. Omelekhina, Y.; Eriksson, A.; Canonaco, F.; Prevot, A.S.H.; Nilsson, P.; Isaxon, C.; Pagels, J.; Wierzbicka, A. Cooking and electronic cigarettes leading to large differences between indoor and outdoor particle composition and concentration measured by aerosol mass spectrometry. *Environ. Sci. Process. Impacts* **2020**, *22*, 1382–1396. [CrossRef]
23. Xiang, J.; Hao, J.; Austin, E.; Shirai, J.; Seto, E. Residential cooking-related PM2.5: Spatial-temporal variations under various intervention scenarios. *Build. Environ.* **2021**, *201*, 108002. [CrossRef]

24. Whitty, C. Executive Summary. In *Chief Medical Officer's Annual Report 2022: Air Pollution*; 2022; pp. i–xix. Available online: https://assets.publishing.service.gov.uk/government/uploads/system/uploads/attachment_data/file/1121614/chief-medical-officers-annual-report-2022-air-pollution.pdf (accessed on 15 November 2024).
25. Anon. Air Pollution Research and Innovation. In *Chief Medical Officer's Annual Report 2022: Air Pollution*; 2022; Chapter 7, pp. 305–308. Available online: https://assets.publishing.service.gov.uk/government/uploads/system/uploads/attachment_data/file/1121614/chief-medical-officers-annual-report-2022-air-pollution.pdf (accessed on 15 November 2024).
26. Qingyang, L.; Joo, S.; Wood, N.; Senerat, A.; Jovan, P. Healthy home interventions: Distribution of PM2.5 emitted during cooking in residential settings. *Build. Environ.* **2021**, *207*, 108448. [CrossRef]
27. Lyu, J.; Shi, Y.; Chen, C.; Zhang, X.; Chu, W.; Lian, Z. Characteristics of PM2.5 emissions from six types of commercial cooking in Chinese cities and their health effects. *Environ. Pollut.* **2022**, *313*, 120180. [CrossRef]
28. Wang, A.; Zhang, Y.; Sun, Y.; Wang, X. Experimental study of ventilation effectiveness and air velocity distribution in an aircraft cabin mockup. *Build. Environ.* **2008**, *43*, 337–343. [CrossRef]
29. Khosravi, G. Prediction of Bioparticles Dispersion and Distribution in a Hospital Isolation Room. Master's Thesis, École de Technologie Supérieure ÉTS, Montreal, QC, Canada, 2016. Available online: https://espace.etsmtl.ca/id/eprint/1631/ (accessed on 15 November 2024).
30. Wang, J.X.; Cao, X.; Chen, Y.P. An air distribution optimization of hospital wards for minimizing cross-infection. *J. Clean. Prod.* **2020**, *279*, 123431. [CrossRef] [PubMed]
31. Armand, P.; Tâche, J. 3D modelling and simulation of the dispersion of droplets and drops carrying the SARS-CoV-2 virus in a railway transport coach. *Sci. Rep.* **2022**, *12*, 4025. [CrossRef] [PubMed]
32. Baker, M.C.; Kong, B.; Capecelatro, J.; Desjardins, O.; Fox, R.O. Direct comparison of Eulerian–Eulerian and Eulerian–Lagrangian simulations for particle-laden vertical channel flow. *AIChE J.* **2020**, *66*, e16230. [CrossRef]
33. Minier, J.P.; Peirano, E. The pdf approach to turbulent polydispersed two-phase flows. *Phys. Rep.* **2001**, *352*, 1–214. [CrossRef]
34. Minier, J.P.; Chibbaro, S.; Pope, S.B. Guidelines for the formulation of Lagrangian stochastic models for particle simulations of single-phase and dispersed two-phase turbulent flows. *Phys. Fluids* **2014**, *26*, 113303. [CrossRef]
35. Zhang, Z.; Chen, Q. Comparison of the Eulerian and Lagrangian methods for predicting particle transport in enclosed spaces. *Atmos. Environ.* **2007**, *41*, 5236–5248. [CrossRef]
36. Tominaga, Y.; Wang, L.L.; Zhai, Z.J.; Stathopoulos, T. Accuracy of CFD simulations in urban aerodynamics and microclimate: Progress and challenges. *Build. Environ.* **2023**, *243*, 110723. [CrossRef]
37. Davies, H.L.; O'Leary, C.; Dillon, T.; Shaw, D.R.; Shaw, M.; Mehra, A.; Phillips, G.; Carslaw, N. A measurement and modelling investigation of the indoor air chemistry following cooking activities. *Environ. Sci. Process. Impacts* **2023**, *25*, 1532–1548. [CrossRef]
38. Zhang, Q.; Gangupomu, R.H.; Ramirez, D.; Zhu, Y. Measurement of Ultrafine Particles and Other Air Pollutants Emitted by Cooking Activities. *Int. J. Environ. Res. Public Health* **2010**, *7*, 1744–1759. [CrossRef]
39. TNO. Health Effects in EU from Cooking on Gas: Phase 2 Field Study. 2023. Available online: https://publications.tno.nl/publication/34641471/zD0Xiz/TNO-2023-R11809.pdf (accessed on 15 November 2024).
40. Lebel, E.D.; Finnegan, C.J.; Ouyang, Z.; Jackson, R.B. Methane and NOx Emissions from Natural Gas Stoves, Cooktops, and Ovens in Residential Homes. *Environ. Sci. Technol.* **2022**, *56*, 2529–2539. [CrossRef] [PubMed]
41. Gill Instruments. WindSonic M Datasheet. 2024. Available online: https://gillinstruments.com/wp-content/uploads/2024/08/1405-0029-WindSonicM-issue-16.pdf (accessed on 15 November 2024).
42. Izadyar, N.; Miller, W.; Rismanchi, B.; Garcia-Hansen, V. A numerical investigation of balcony geometry impact on single-sided natural ventilation and thermal comfort. *Build. Environ.* **2020**, *177*, 106847. [CrossRef]
43. Omrani, S.; Garcia-Hansen, V.; Capra, B.R.; Drogemuller, R. Effect of natural ventilation mode on thermal comfort and ventilation performance: Full-scale measurement. *Energ. Build.* **2017**, *156*, 1–16. [CrossRef]
44. QuantAQ. QuantAQ: MODULAIR-PM (Product Datasheet). 2021. Available online: https://assets.quant-aq.com/downloads/spec-sheets/modulair-pm.latest.pdf (accessed on 15 November 2024).
45. AQMD. South Coast Air Quality Management District: QuantAQ MODULAIR-PM Sensor Detail and Field Evaluation. 2021. Available online: http://www.aqmd.gov/aq-spec/sensordetail/quantaq---modulair-pm (accessed on 15 November 2024).
46. AirSentric. AirSentric WB55 AR10-B-118-A Technical Specification. 2022. Available online: https://airsentric.com/wb55-118-specifications/ (accessed on 15 November 2024).
47. Zheng, H.; Krishnan, V.; Walker, S.; Loomans, M.; Zeiler, W. Laboratory evaluation of low-cost air quality monitors and single sensors for monitoring typical indoor emission events in Dutch daycare centers. *Environ. Int.* **2022**, *166*, 107372. [CrossRef]
48. O'Leary, C.; de Kluizenaar, Y.; Jacobs, P.; Borsboom, W.; Hall, I.; Jones, B. Investigating measurements of fine particle (PM2.5) emissions from the cooking of meals and mitigating exposure using a cooker hood. *Indoor Air* **2019**, *29*, 423–438. [CrossRef]
49. Harding-Smith, E.; Davies, H.L.; O'Leary, C.; Winkless, R.; Shaw, M.; Dillon, T.; Jones, B.; Carslaw, N. The impact of surfaces on indoor air chemistry following cooking and cleaning. *Environ. Sci. Process. Impacts* **2024**. [CrossRef]
50. Jones, H.; Kumar, A.; O'Leary, C.; Dillon, T.; Rolfo, S. Experimental and Computational Investigation of the Emission and Dispersion of Fine Particulate Matter (PM2.5) During Domestic Cooking—Dataset. *eData* **2024**. [CrossRef]
51. Chibbaro, S.; Minier, J.P. Langevin PDF simulation of particle deposition in a turbulent pipe flow. *J. Aerosol Sci.* **2008**, *39*, 555–571. [CrossRef]

52. Balvet, G.; Minier, J.P.; Henry, C.; Roustan, Y.; Ferrand, M. A time-step-robust algorithm to compute particle trajectories in 3D unstructured meshes for Lagrangian stochastic methods. *Monte Carlo Methods Appl.* **2023**, *29*, 95–126. [CrossRef]
53. Minier, J.P.; Peirano, E.; Chibbaro, S. PDF model based on Langevin equation for polydispersed two-phase flows applied to a bluff-body gas-solid flow. *Phys. Fluids* **2004**, *16*, 2419–2431. [CrossRef]
54. CEA; EDF; OPEN CASCADE. SALOME Platform Documentation. 2023. Available online: https://docs.salome-platform.org/latest/main/index.html (accessed on 15 November 2024).
55. Archambeau, F.; Méchitoua, N.; Sakiz, M. Code Saturne: A Finite Volume Code for the computation of turbulent incompressible flows—Industrial Applications. *Int. J. Finite Vol.* **2004**, *1*. hal-01115371.
56. Fournier, Y.; Bonelle, J.; Moulinec, C.; Shang, Z.; Sunderland, A.; Uribe, J. Optimizing Code_Saturne computations on Petascale systems. *Comput. Fluids* **2011**, *45*, 103–108. [CrossRef]
57. EDF R&D. Code_Saturne 8.0 Theory Guide. 2022. Available online: https://www.code-saturne.org/documentation/8.0/theory.pdf (accessed on 15 November 2024).
58. Gray, D.D.; Giorgini, A. The validity of the boussinesq approximation for liquids and gases. *Int. J. Heat Mass Tran.* **1976**, *19*, 545–551. [CrossRef]
59. Manceau, R.; Hanjalić, K. Elliptic blending model: A new near-wall Reynolds-stress turbulence closure. *Phys. Fluids* **2002**, *14*, 744–754. [CrossRef]
60. Germano, M.; Piomelli, U.; Moin, P.; Cabot, W.H. A dynamic subgrid-scale eddy viscosity model. *Phys. Fluids A Fluid Dyn.* **1991**, *3*, 1760–1765. [CrossRef]
61. Ducros, F.; Franck, N.; Poinsot, T. Wall-Adapting Local Eddy-Viscosity Models for Simulations in Complex Geometries. In the Conference Proceedings Numerical Methods for Fluid Dynamics VI. 1998. Available online: https://www.researchgate.net/publication/248366844_Wall-Adapting_Local_Eddy-Viscosity_Models_for_Simulations_in_Complex_Geometries (accessed on 15 November 2024).
62. Ayachit, U. *The ParaView Guide: A Parallel Visualization Application*; Kitware: New York, NY, USA, 2015; ISBN 9781930934306.
63. Pikmann, J.; Drewnick, F.; Fachinger, F.; Borrmann, S. Particulate emissions from cooking activities: Emission factors, emission dynamics, and mass spectrometric analysis for different preparation methods. *EGUsphere* **2023**, *2023*, 1–36. [CrossRef]
64. Wang, P.; Xu, F.; Gui, H.; Wang, H.; Chen, D.R. Effect of Relative Humidity on the Performance of Five Cost-effective PM Sensors. *Aerosol Sci. Tech.* **2021**, *55*, 957–974. [CrossRef]
65. Willeke, K.; Whitby, K.T. Atmospheric Aerosols: Size Distribution Interpretation. *J. Air Pollut. Control Assoc.* **1975**, *25*, 529–534. [CrossRef]
66. Farghadan, A.; Poorbahrami, K.; Jalal, S.; Oakes, J.M.; Coletti, F.; Arzani, A. Particle transport and deposition correlation with near-wall flow characteristic under inspiratory airflow in lung airways. *Comp. Biol. Med.* **2020**, *120*, 103703. [CrossRef]
67. Li, C.; Crua, C.; Vogiatzaki, K. Effect of the scale resolution on the two phase coupling characteristics of high speed evaporating sprays using LES / Eulerian-Lagrangian methodologies. *Int. J. Multiphas. Flow* **2019**, *120*, 103060. [CrossRef]
68. Courant, R.; Friedrichs, K.; Lewy, H. On the Partial Difference Equations of Mathematical Physics. *IBM J. Res. Dev.* **1967**, *11*, 215–234. [CrossRef]

Disclaimer/Publisher's Note: The statements, opinions and data contained in all publications are solely those of the individual author(s) and contributor(s) and not of MDPI and/or the editor(s). MDPI and/or the editor(s) disclaim responsibility for any injury to people or property resulting from any ideas, methods, instructions or products referred to in the content.